ACS APPLIED ENERGY MATERIALS

www.acsaem.org Article

Computational Understandings of Cation Configuration-Dependent Redox Activity and Oxygen Dimerization in Lithium-Rich Manganese-Based Layered Cathodes

Zhenming Xu, Junwu Tian, Zhi Dou, Mingbo Zheng,* Yixi Lin, Huiyu Duan, Hong Zhu,* and Yongyao Xia*

Cite This: https://doi.org/10.1021/acsaem.3c00480 Read Online

ACCESS | Metrics & More | Article Recommendations | Supporting Information

ABSTRACT: Lithium-rich manganese-based layered oxides have emerged as a fresh paradigm for developing advanced cathode materials with high energy density for next-generation lithium-ion batteries. Understanding lattice oxygen dimerization is quite essential for the optimal design of lithium-rich manganese-based cathode materials. Herein, based on density functional theory (DFT) calculations, a local Ni-honeycomb Li−Ni−Mn cation configuration for the $Li_{1.22}Ni_{0.22}Mn_{0.56}O_2$ cathode was carefully examined, which may coexist with the well-known local Li-honeycomb structure in experimentally synthesized $Li_{1.2}Ni_{0.2}Mn_{0.6}O_2$ samples. The local Li−Ni−Mn cation configurations have significant impacts on oxygen redox activity, transition metal atom migration, and oxygen dimerization in the charging process of $Li_xNi_{0.22}Mn_{0.56}O_2$. It is found that there is no correlation between high lattice oxygen redox activity and easy oxygen dimerization, such as Li-honeycomb structures simultaneously exhibiting higher oxygen redox activities and higher activation energy barriers for prohibiting oxygen dimerization than Ni-honeycomb structures. The structural regulations of the local Li−Ni−Mn cation configuration by avoiding the local Ni-honeycomb structures to inhibit Mn migration and ease lattice oxygen dimerization and by making full use of the local Li-honeycomb structures would maximize performance of Li-rich Mn-based layered oxides. Such fresh insights provide us a fresh strategy to optimally design the local honeycomb structure for high-performance Li-rich Mn-based cathode materials.

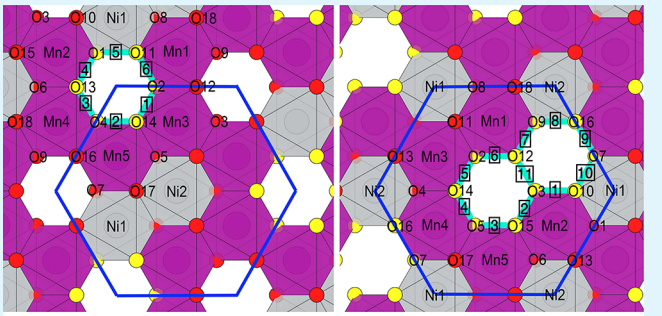

KEYWORDS: *Li-rich Mn-based cathode, Li-honeycomb, cation configuration, lattice oxygen activity, oxygen dimerization*

1. INTRODUCTION

Lithium-ion batteries (LIBs) are currently the primary source of portable energy storage for powering mobile phone and electric vehicles.[1−3] However, the energy density of the current LIBs is quite overstretched for large-scale energy-storage applications. Recently, anionic oxygen redox has been identified to provide additional (de)intercalation capacity in some Li-rich Mn-based cathode materials,[4,5] with a chemical formula of $xLi_2MnO_3{\cdot}(1-x)LiMO_2$ (M = Ni, Co and Mn), meeting the energy density demands of next-generation technologies. Nonetheless, almost all oxygen-redox-active materials universally show irreversible electrochemical performances, such as first-cycle voltage hysteresis and capacity degradation.[6,7] It is the biggest obstacle for the ultimate commercialization of Li-rich Mn-based layered cathode materials. Usually, phase change resulting from the displacement of transition metal (TM) atoms into the alkali metal layer and microstructural defects caused by oxygen release during first charge are regarded as the two main reasons for the first-cycle voltage hysteresis and capacity degradation.[4,8,9] Therefore, deep understanding of the phase change and oxygen evolution in Li-rich cathodes and proposing effective strategies to suppress these negative factors are very essential for commercial application of Li-rich Mn-based layered cathode materials.

First-principles calculation based on the density functional theory (DFT) is a low-cost and powerful tool for probing into the physical mechanism and understanding the electrochemical performance of battery materials at the electronic and atomic scales,[10,11] which are not available for the current experimental techniques. Ceder and co-workers have reported that an

Received: February 21, 2023
Accepted: May 15, 2023

unhybridized O-2p electron state associated with the special Li−O−Li configuration in Li-rich cathodes is the chemical and structural origin of oxygen redox activity[12] which has been widely accepted by the battery community. In Li-rich cathode materials, density of states (DOSs) of the O-2p state near the Fermi level are usually close to and even more than those of TM-3d states,[13,14] and there is an unhybridized O-2p state near the Fermi level.[12] Therefore, anionic redox reaction would occur simultaneously or subsequent to cationic redox reaction specifically depending on the 3d state of TM cations. After charging to some extent, oxygen ions with holes spontaneously hybridize with other adjacent oxygen ions, forming O−O dimers.[15] Oxygen dimerization with low kinetic barriers eventually leads to the formation and release of molecular O_2 and the irreversible displacement of TM atoms into the alkali metal layer.[16,17] Note that oxygen dimerization needs two neighboring oxidized oxygen ions to rotate themselves to overlap their 2p orbitals,[16,18] and thus the feasibility of oxygen dimerization depends on the coordination environment around oxygen. The weak TM−O hybridizations and oxygen surrounded by more non-TMs would facilitate oxygen dimerization.[19]

Recent research studies show that the oxygen redox chemistry of Li(Na)-rich cathode materials is not only regulated by TM species[19,20] but also effectively modulated by cation configurations in the TM layer.[18,21,22] Bruce and co-workers compared two closely related intercalation cathodes by experimental characterizations and DFT calculations, $Na_{0.75}[Li_{0.25}Mn_{0.75}]O_2$ with the honeycomb superstructure and $Na_{0.6}[Li_{0.2}Mn_{0.8}]O_2$ with the ribbon superstructure, and they found that the first-cycle voltage hysteresis is significantly determined by the local configurations of Li−Mn in TM layers.[21] Xia and co-workers found that tuning the local symmetry around oxygen ions can inhibit O−O dimerization for oxygen redox reaction in Li_2RuO_3, enabling significantly enhanced cycling stability and negligible voltage decay.[23] Chen et al. experimentally revealed that the Li/Ni disorder and the Li vacancy can inhibit the formation of O_2^- and O_2^{2-} dimers in $Li_{1.19}Ni_{0.26}Mn_{0.55}O_2$.[22] In addition, the three-dimensional (3D)-disordered cation framework of $Li_{1.2}Ti_{0.35}Ni_{0.35}Nb_{0.1}O_{1.8}F_{0.2}$ can stabilize lattice oxygen redox compared to two-dimensional/3D-ordered cation structures.[18] We also noticed a previous DFT work of studying the role of dopant metal atoms on the structural and electronic properties of $Li_{1.2}Ni_{0.2}Mn_{0.6}O_2$.[24] In that work, two cation ordering models for Li, Mn, and Ni configurations in the Li−Ni−Mn mixed layer were considered, in which Li and Ni were separated by one Mn atom in each row (model-1) and Li and Ni adopted neighboring sites in each row (model-2). Although the proposed $Li_{1.2}Ni_{0.2}Mn_{0.6}O_2$ models have the same compositions as experimental materials, both Li and Ni atoms in the Li−Ni−Mn mixed layer show ordering rodlike configurations, which possess much higher electrostatic repulsive interactions than other Li−Ni−Mn configurations without ordering rodlike patterns.[25,26]

For the most representative Li-rich Mn-based cathode material possessing high voltage and high specific capacity, $Li_{1.2}Ni_{0.2}Mn_{0.6}O_2$,[27−29] to the best of our knowledge, how Li−Ni−Mn cation configurations affect oxygen redox activity and oxygen dimerization has not been extensively explored, except for the experimental studies of Li/Ni disorder and Li vacancy by Chen and co-workers.[22] Therefore, in this work, we investigated the relationship among Li−Ni−Mn cation configuration, lattice oxygen redox activity, and oxygen dimerization in $Li_{1.22}Ni_{0.22}Mn_{0.56}O_2$ at the electronic and atomic scales by DFT calculations and identified the mechanism of Ni-honeycomb cation configuration aggravating lattice oxygen dimerization.

2. COMPUTATIONAL METHODOLOGIES

All calculations were performed by using the projector augmented wave method in the framework of the DFT,[30] as implemented in the Vienna ab-initio Simulation Package. The Perdew−Burke−Ernzerhof exchange functional[31] in the framework of generalized gradient approximation (GGA)[32] was utilized to solve the Schrödinger's equation of the quantum states of electrons. Energy cutoff of plane-wave is 500 eV. Convergence criteria of energy and force are 10^{-5} eV/atom and 0.01 eV/Å, respectively. The number of *k*-points was 2000 divided by the number of atoms in the unit cell. Geometry optimizations and electronic structures were calculated by using the spin-polarized GGA plus Hubbard correction U (GGA + U) method.[33] Hubbard U parameters of Mn and Ni elements are 4.9 and 6.0 eV, respectively.[34] $Li_{1.22}Ni_{0.22}Mn_{0.56}O_2$ models were constructed from the $LiCoO_2$ primitive cell (space group: $R\bar{3}m$) with determined Li−Ni−Mn configurations in the Co atomic layer. For the exact composition of $Li_{1.2}Ni_{0.2}Mn_{0.6}O_2$, a 5 × 5 × 1 supercell with 100 atoms needs to be created, which would greatly increase the computational burden, especially for the hybrid functional calculation. Weighting the computational accuracy and burden, we chose a close composition of $Li_{1.22}Ni_{0.22}Mn_{0.56}O_2$ to represent a common Li-rich Mn-based $Li_{1.2}Ni_{0.2}Mn_{0.6}O_2$ cathode material, which just needs a 3 × 3 × 1 supercell with 36 atoms. A total of 28 Li−Ni−Mn cation configurations in the TM layer were created within a 3 × 3 × 1 supercell of the $LiCoO_2$ primitive cell using the enumeration method[35] as implemented in the Pymatgen code.[36] The Li−Ni−Mn cation configuration of the most stable $Li_{1.22}Ni_{0.22}Mn_{0.56}O_2$ structure was determined by ranking 28 Li−Ni−Mn cation configurations by their DFT energies. Moreover, the delithiated structures with Li-vacancy orderings were also enumerated by the Pymatgen code. The activation energy barriers of oxygen dimer formation were calculated by the nudged elastic band (NEB) method,[37] and GGA + U effects were also considered for NEB calculations. Crystal orbital Hamilton population (COHP) between neighboring oxygen atoms were computed by the Lobster program,[38] in which the negative and positive COHP values indicate bonding and antibonding, respectively. Atomic charges were calculated from the charge density grid using the Bader charge analysis code.[39]

3. RESULTS AND DISCUSSION

Traditionally, Li-rich Mn-based layered $Li_{1.2}Ni_{0.2}Mn_{0.6}O_2$ material is regarded as the two-phase composite model[40,41] or the single-phase solid solution model[42,43] of $R\bar{3}m$-$LiNi_{0.5}Mn_{0.5}O_2$ and $C2/m$-Li_2MnO_3. In a massive previous work, X-ray diffraction (XRD) patterns of $Li_{1.2}Ni_{0.2}Mn_{0.6}O_2$ were usually matched to $R\bar{3}m$-$LiNi_{0.5}Mn_{0.5}O_2$ and $C2/m$-Li_2MnO_3, especially for the (003) peak of $R\bar{3}m$-$LiNi_{0.5}Mn_{0.5}O_2$, the (020) and (110) peaks of $C2/m$-Li_2MnO_3.[44−47] On the other hand, it is usually believed that layered $Li_{1.2}Ni_{0.2}Mn_{0.6}O_2$ is composed of pure lithium layers fully filled with lithium ions and Li−Ni−Mn mixed atomic layers with a molar ratio of 1:1:3,[48,49] as shown in Figure S1. However, this mixed layer

https://doi.org/10.1021/acsaem.3c00480
ACS Appl. Energy Mater. XXXX, XXX, XXX−XXX

model with fractional atom occupation cannot be directly processed by molecular simulation and DFT calculation. Therefore, it is necessary to deal with fractional atom occupation of $Li_{1.2}Ni_{0.2}Mn_{0.6}O_2$ and determine the most stable Li−Ni−Mn cation configuration. Replacing Co atoms in the 5 × 5 × 1 supercell of the $LiCoO_2$ primitive cell with Li:Ni:Mn = 1:1:3 would obtain structure models of $Li_{1.2}Ni_{0.2}Mn_{0.6}O_2$ with its exact stoichiometric ratio, but there are about 10^{16} Li−Ni−Mn cation configurations, so it is a big disaster for enumerating the structure and DFT calculation. Weighting the computational accuracy and burden, we chose a much close composition of $Li_{1.22}Ni_{0.22}Mn_{0.56}O_2$ to model the $Li_{1.2}Ni_{0.2}Mn_{0.6}O_2$ compound. There are 11 Li, 2 Ni, 5 Mn, and 18 O atoms in the supercell model of $Li_{1.22}Ni_{0.22}Mn_{0.56}O_2$, in which 2 out of 11 Li atoms are in TM mixed layers and 9 out of 11 Li atoms are in pure lithium layers. All possible Li−Ni−Mn cation configurations are enumerated by considering the structure symmetry. Both lattice constants and atomic positions of the enumerated structures were optimized, and subsequently their Ewald electrostatic and DFT energies were calculated, as shown in Figure S2. Both electrostatic potentials and DFT calculated energies of enumerated 28 $Li_{1.22}Ni_{0.22}Mn_{0.56}O_2$ structures consistently show that it is favorable for the formation of Li-honeycomb configuration in the TM layer (Figure 1a), which is similar to Li_2TMO_3 with

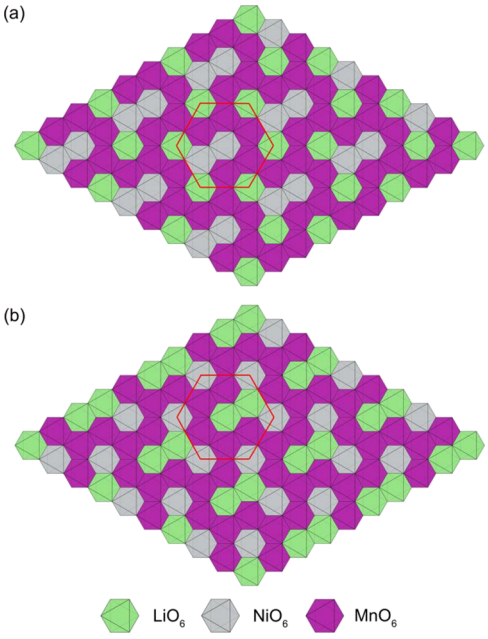

Figure 1. Crystal structures of layered $Li_{1.22}Ni_{0.22}Mn_{0.56}O_2$. Top views of the (a) most stable and (b) second most stable $Li_{1.22}Ni_{0.22}Mn_{0.56}O_2$ with the Li-honeycomb and Ni-honeycomb Li−Ni−Mn configurations, respectively. Crystal structures are displayed by VESTA software.[55]

perfect honeycomb Li-TM ordering.[50,51] Moreover, honeycomb Li-Mn patterns are also observed in $Na_{0.67}[Li_{0.22}Mn_{0.78}]O_2$,[52] whose stoichiometric ratio of 0.22:0.78 is as the same as Li:TM = 0.22:(0.22 + 0.56) of our $Li_{1.22}Ni_{0.22}Mn_{0.56}O_2$ model.

Energy difference between the ground-state Li-honeycomb structure and the second most stable Ni-honeycomb structure (Figure 1b) is relatively small, just ∼24 meV/atom. Such a small energy difference is almost equal to k_BT of ∼26 meV/atom at room temperature, and it indicates that the local Li-honeycomb and Ni-honeycomb cation configurations likely coexist in the experimentally synthesized samples. These two specific Li-honeycomb and Ni-honeycomb orderings would lower the atomic density of Li or TM in space and eventually reduce electrostatic repulsive potentials among Li or TM ions. Furthermore, the simulated XRD patterns for Li-honeycomb and Ni-honeycomb $Li_{1.22}Ni_{0.22}Mn_{0.56}O_2$ structures (Figure S3) clearly show that the diffraction intensity of Ni-honeycomb structures at ∼20.8° is stronger than that at ∼21.8°, which is closer to the experimentally determined data of $Li_{1.2}Ni_{0.2}Mn_{0.6}O_2$.[28,53,54] Both DFT-calculated energies and simulated XRD data demonstrate that the local Ni-honeycomb structure as an important domain would probably appear in experimentally synthesized $Li_{1.2}Ni_{0.2}Mn_{0.6}O_2$ together with the local Li-honeycomb structures, and it deserves more attention from the experimentalist. Therefore, in this theoretical work, we mainly focused on the local Li-honeycomb and Ni-honeycomb structured $Li_{1.22}Ni_{0.22}Mn_{0.56}O_2$ to deepen our understanding of the Li−Ni−Mn cation configurations affecting oxygen redox activity and oxygen dimerization in lithium-rich manganese-based layered cathodes. On the other hand, it should be noted that because of the periodic boundary condition and the limited supercell size, the Li-honeycomb and Ni-honeycomb structures in the $Li_{1.22}Ni_{0.22}Mn_{0.56}O_2$ model are long-ranged, but the Li-honeycomb and Ni-honeycomb structures in the $Li_{1.2}Ni_{0.2}Mn_{0.6}O_2$ compound should be short-ranged and local, that is, the so-called domains. These different honeycomb ranges come from a small composition difference between the $Li_{1.22}Ni_{0.22}Mn_{0.56}O_2$ model and the $Li_{1.2}Ni_{0.2}Mn_{0.6}O_2$ compound, but it does not affect our qualitative analysis of Li−Ni−Mn cation configuration-dependent lattice oxygen redox activity and oxygen dimerization in the $Li_{1.2}Ni_{0.2}Mn_{0.6}O_2$ compound by using the $Li_{1.22}Ni_{0.22}Mn_{0.56}O_2$ model.

3.1. Structural Evolutions upon Delithiation. By sufficient DFT calculations for all Li-vacancy configurations in the supercell model, the ground-state structures of a cathode material at different delithiation levels can be determined, which contribute to our understandings of structural evolution during the charge and discharge processes. The ground-state structures of delithiated $Li_xNi_{0.22}Mn_{0.56}O_2$ with the Li-honeycomb and Ni-honeycomb Li−Ni−Mn configurations were determined by calculating and ranking their DFT formation energies at each lithium concentration, and the corresponding results are shown in Figures 2, S4 and S5. Viewed from Figure 2a,b, the lowest energy of delithiated structures at each delithiation concentration constitutes convex hulls (green lines), which means our Li−Ni−Mn configuration spaces (enumerated Li−Ni−Mn configurations) are sufficient to model the $Li_{1.22}Ni_{0.22}Mn_{0.56}O_2$ structure. Because of the size limitations of the supercell and the composition difference between DFT models of $Li_{1.22}Ni_{0.22}Mn_{0.56}O_2$ and the experimental structure of $Li_{1.2}Ni_{0.2}Mn_{0.6}O_2$, DFT ground-state structures of delithiated $Li_xNi_{0.22}Mn_{0.56}O_2$ (Figures S4 and S5) cannot strictly represent the actual crystal structures upon delithiation step by step in experiments, but they are competent for showing general patterns of the structural evolution of lithium configurations during charge and discharge process.

Both for the Li-honeycomb and Ni-honeycomb structured $Li_{11-x}Ni_2Mn_7O_{18}$, it is found that at the initial charge stage (x = 1, 2, and 3), the extracted Li ions come from the pure lithium layer, and Li ions in the Li−Ni−Mn mixed layer still reside at

https://doi.org/10.1021/acsaem.3c00480
ACS Appl. Energy Mater. XXXX, XXX, XXX−XXX

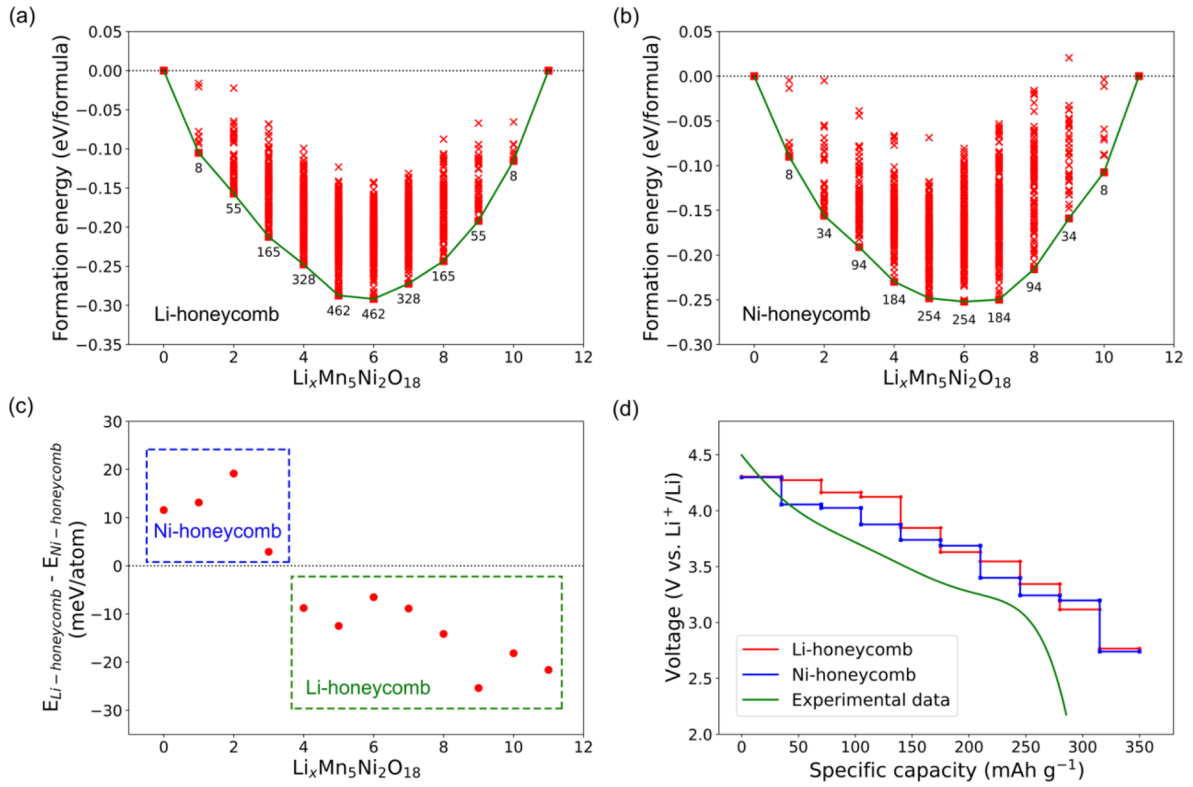

Figure 2. DFT-calculated formation energies of a 3 × 3 × 1 supercell for delithiated $Li_{1.22}Ni_{0.22}Mn_{0.56}O_2$ with the (a) Li-honeycomb and (b) Ni-honeycomb Li−Ni−Mn configurations. The numbers labeled below the ground-state line are the total number of these enumerated structures with DFT energies at each lithium concentration. (c) Relative energy difference between Li-honeycomb and Ni-honeycomb structured $Li_xNi_{0.22}Mn_{0.56}O_2$ at different delithiation levels (data in the dotted line box denote the stable phase at different delithiation levels). (d) Intercalation voltage profiles of Li-honeycomb and Ni-honeycomb structured $Li_{1.22}Ni_{0.22}Mn_{0.56}O_2$ at different delithiation levels. Green line represents the experimental data of $Li_{1.2}Ni_{0.2}Mn_{0.6}O_2$ from the previous work.[28]

their lattice sites (Figures S4a−S4c and S5a−S5c). In addition, the layer distance gradually increases upon delithiation during this initial charge stage (Figure S6). On further charging, the Li ions in the Li−Ni−Mn mixed layer are extracted at x = 4 and 5. Meanwhile, some Li ions in the pure Li layer begin to occupy the tetrahedral sites upon delithiation at x = 4 and 5, making the layer distance further increase. When charging to x = 6 and 7, tetrahedral Li ions in the pure Li layer are further extracted from the lattice structure, so the corresponding layer distance decreases. At the last charge stage (x = 8, 9, 10, and 11), the layer distances significantly reduce with remaining Li ions extracted. In sum, the layer distances of $Li_{1.22}Ni_{0.22}Mn_{0.56}O_2$ first increase and then decrease upon delithiation. This variation is fully consistent with the previous experimental work of $Li_{1.2}Ni_{0.2}Mn_{0.6}O_2$[28] but is quite different from that of $LiCoO_2$,[56,57] which may be because of the appearance and disappearance of tetrahedral Li ions during the charge process.

Figure 2c shows the relative energy difference between the Li-honeycomb and Ni-honeycomb structured $Li_xNi_{0.22}Mn_{0.56}O_2$ at different delithiation levels, and it can be seen that the absolute values of the relative energy difference between the two phases are less than 30 meV/atom, close to k_BT of ∼26 meV/atom at room temperature, indicating a small difference of thermodynamic stability. Moreover, energies of Li-honeycomb $Li_xNi_{0.22}Mn_{0.56}O_2$ (x > 0.4) structures are slightly lower than those of the corresponding Ni-honeycomb structures, which are similar to the fully lithiated $Li_{1.22}Ni_{0.22}Mn_{0.56}O_2$ structures. Based on delithiated structures, we calculated the intercalation voltage profiles of the Li-honeycomb and Ni-honeycomb structured $Li_{1.22}Ni_{0.22}Mn_{0.56}O_2$, as shown in Figure 2d. It can be seen that the Ni-honeycomb structure shows relatively lower voltage profiles and average voltage value than the Li-honeycomb structures, and the voltage profiles of the Ni-honeycomb structured $Li_{1.22}Ni_{0.22}Mn_{0.56}O_2$ are closer to the experimental data of $Li_{1.2}Ni_{0.2}Mn_{0.6}O_2$.[28] It proves again that Ni-honeycomb structures would coexist with the ground-state Li-honeycomb structures in experimentally synthesized $Li_{1.2}Ni_{0.2}Mn_{0.6}O_2$.

3.2. Redox Reactions upon Delithiation. Electronic structure analyses are effective tools to study the redox activity of a cathode material.[13] Element projected density of states (PDOS) in Figure 3a,b clearly shows that the valence band maximum (VBM) of the Li-honeycomb and Ni-honeycomb structured $Li_{1.22}Ni_{0.22}Mn_{0.56}O_2$ is mainly composed of occupied Ni-3d and O-2p spin-up states, that is, the Ni−O anti-bonding state.[58] It indicates that electrons are mainly extracted from Ni-3d and O-2p spin-up states upon delithiation, and nickel and oxygen actively participate in the initial redox reactions. To further visualize the electron's space distributions at the VBM, partial charge densities of the Li-honeycomb and Ni-honeycomb structured $Li_{1.22}Ni_{0.22}Mn_{0.56}O_2$ were calculated, as shown in Figure 3c,d, respectively. As charge density isosurfaces show, the VBM electrons of Li-honeycomb structures mainly localize at Ni and O ions in NiO_6, and a small amount of VBM electrons is observed at those O ions with Li−O−Li configurations (nonbonding O-2p electrons),[12] including O4, O11, and O13, while for Ni-honeycomb structured

https://doi.org/10.1021/acsaem.3c00480
ACS Appl. Energy Mater. XXXX, XXX, XXX−XXX

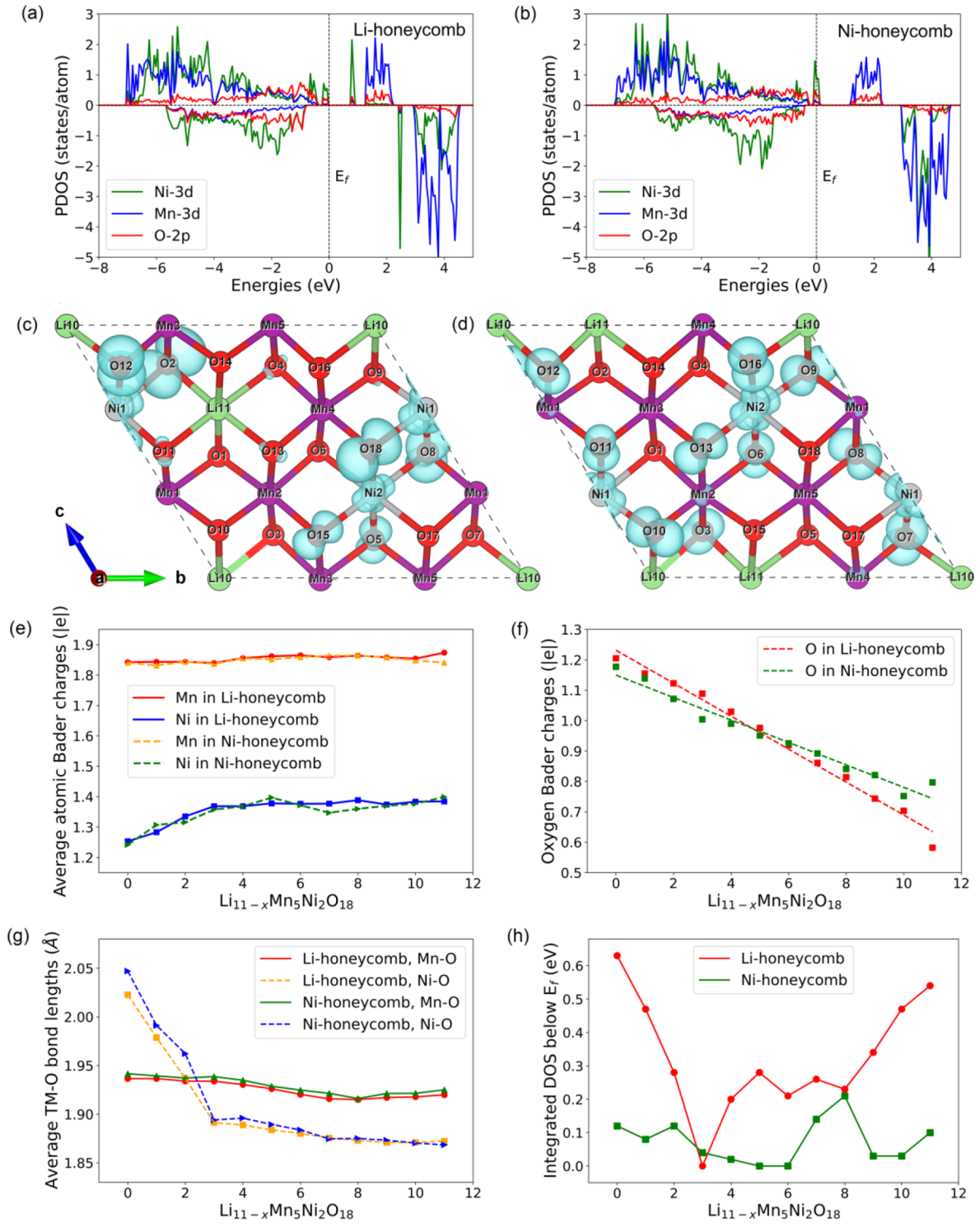

Figure 3. Element PDOS of the (a) Li-honeycomb and (b) Ni-honeycomb structured $Li_{1.22}Ni_{0.22}Mn_{0.56}O_2$. Partial charge densities (light blue isosurfaces) at the VBM of (c) Li-honeycomb and (d) Ni-honeycomb structured $Li_{1.22}Ni_{0.22}Mn_{0.56}O_2$, and the isosurface value is 0.002 e/Å^3; VBM energy windows of [−0.23 eV, 0] and [−0.17 eV, 0] were chosen for partial charge density calculation, respectively, for Li-honeycomb and Ni-honeycomb structures, which correspond to widths of the first DOS peak below E_f. Average atomic Bader charges (in e) of (e) TMs and (f) oxygens (near and far away from the Li vacancy in the Li−Mn−Ni mixed layer) of $Li_xNi_{0.22}Mn_{0.56}O_2$ at different delithiation concentrations. (g) Average TM-O bond lengths and (h) integrated oxygen PDOS below the Fermi energy levels (from −1.0 eV to 0) of $Li_xNi_{0.22}Mn_{0.56}O_2$ at different delithiation concentrations. Crystal structures with isosurfaces are displayed by VESTA software.[55]

$Li_{1.22}Ni_{0.22}Mn_{0.56}O_2$ (Figure 3d), VBM electrons are not only distributed at Ni and O ions in NiO_6 but also considerable isolated O-2p electrons are observed at O3, which is different from those of Li-honeycomb structures. As a whole, Li-honeycomb structured $Li_{1.22}Ni_{0.22}Mn_{0.56}O_2$ has larger isosurface areas (radii) of VBM charge density, especially for O2, O12, and O18. Both from the analyses of PDOS and partial charge density, the occupied electrons near the Fermi energy

https://doi.org/10.1021/acsaem.3c00480
ACS Appl. Energy Mater. XXXX, XXX, XXX−XXX

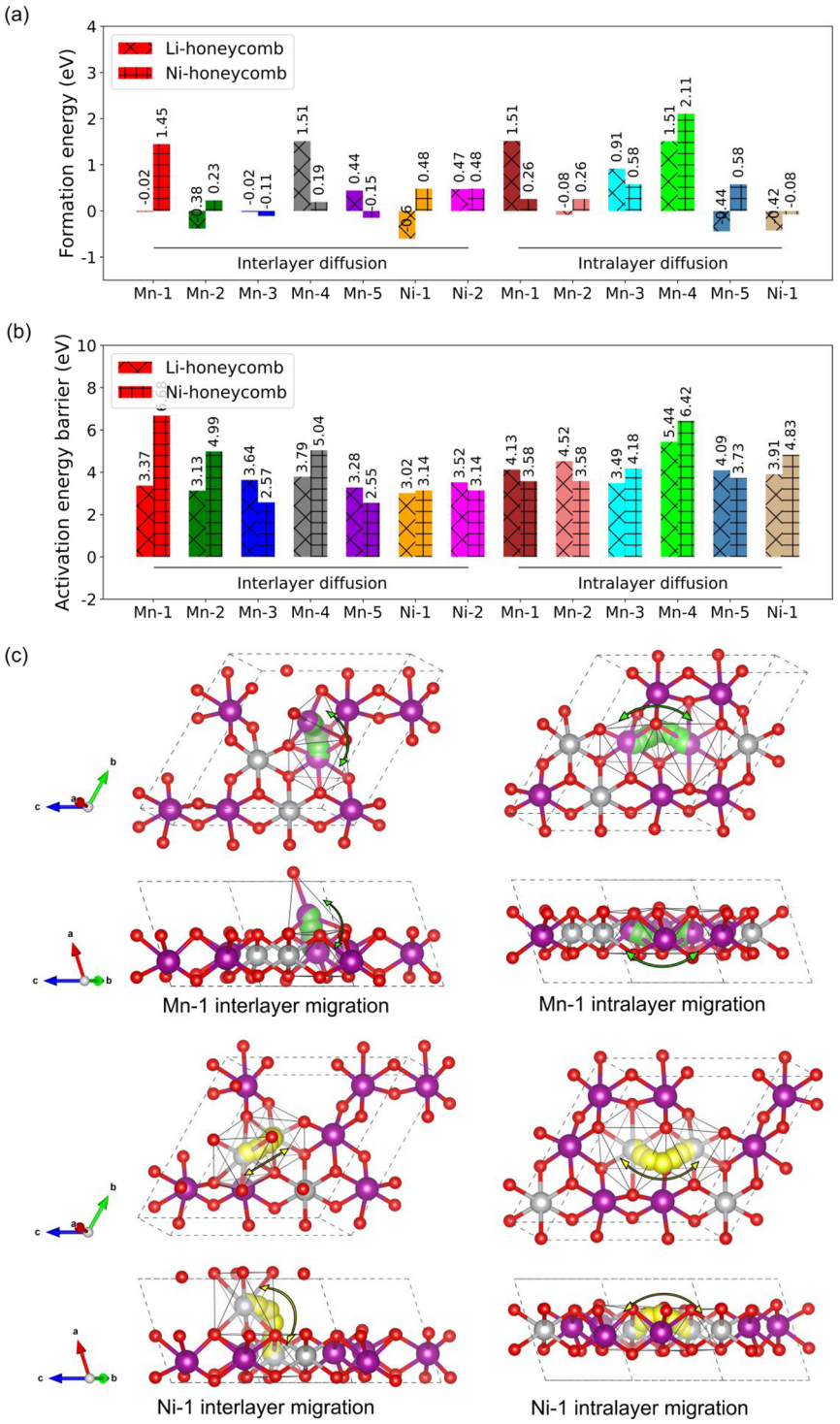

Figure 4. Probability and rate of TM migration in $Ni_{0.22}Mn_{0.56}O_2$. (a) Formation energies and (b) activation energy barriers for Mn and Ni atoms migrating to the adjacent lithium vacancy sites along (c) interlayer and intralayer diffusion directions in the Li-honeycomb structure, respectively. There is no Li vacancy site around Ni-2 atoms in the lithium-TM mixed layer, so Ni-2 atoms have no intralayer diffusion. Mn/Ni migrating trajectories are highlighted in green and yellow colors, respectively. Crystal structures are displayed by VESTA software.[55]

level of Li-honeycomb structured $Li_{1.22}Ni_{0.22}Mn_{0.56}O_2$ are more than those of Ni-honeycomb structures, indicating the higher redox activities of Li-honeycomb structures at the beginning of charging.

Besides the fully lithiated $Li_{1.22}Ni_{0.22}Mn_{0.56}O_2$, PDOSs of delithiated $Li_{11-x}Ni_2Mn_5O_{18}$ (x = 1 to 11) were also calculated to evaluate their oxidation processes upon delithiation, as shown in Figures S7 and S8. It can be seen that with the first lithium extracted from $Li_{11}Ni_2Mn_5O_{18}$ to $Li_{10}Ni_2Mn_5O_{18}$, Fermi energy levels shift to low energy, and local electron states of $Li_{11}Ni_2Mn_5O_{18}$ close to Fermi energy level disappear, exhibiting oxidization of VBM electrons (Figure 3c,d) upon the first-step delithiation. On delithiations from $Li_{10}Ni_2Mn_5O_{18}$ to $Li_9Ni_2Mn_5O_{18}$, Ni and O are further oxidized and band gaps gradually reduce. On further delithiations from $Li_9Ni_2Mn_5O_{18}$ to $Ni_2Mn_5O_{18}$, not only Ni and O are oxidized, but also Mn

https://doi.org/10.1021/acsaem.3c00480
ACS Appl. Energy Mater. XXXX, XXX, XXX−XXX

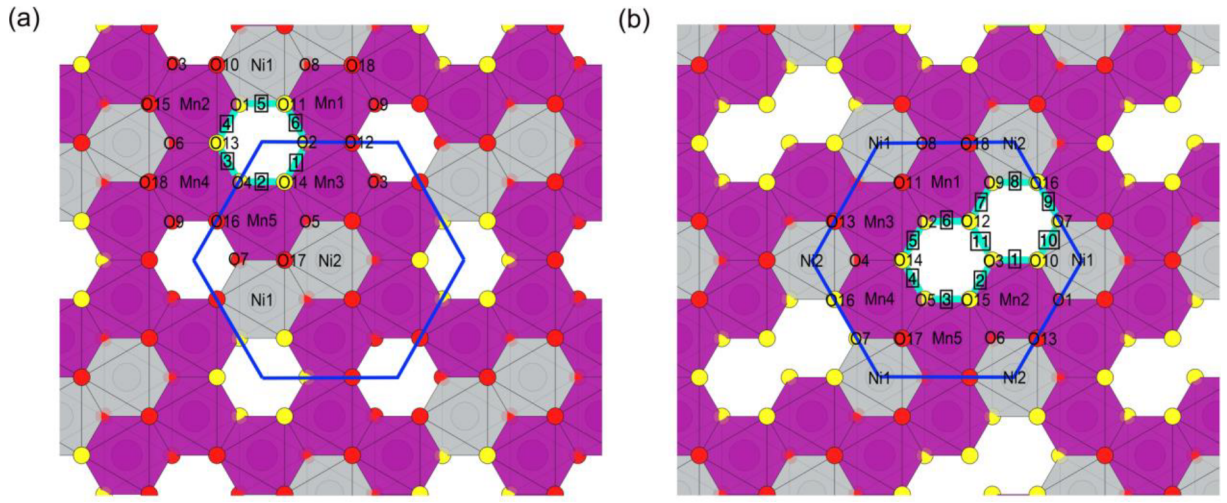

Figure 5. Potential intralayer oxygen dimerization in the Li−Ni−Mn mixed layer (along *c*-axis) of the fully delithiated (a) Li-honeycomb and (b) Ni-honeycomb structured $Ni_{0.22}Mn_{0.56}O_2$. Oxygen ions for dimerization are highlighted in yellow color, and oxygen dimers are labeled with numbers (in rectangular frames, case 1−6 and case 1−11) and highlighted in cyan color. Crystal structures are displayed by VESTA software.[55]

takes part in oxidizations. Atomic Bader charge analyses (Figure 3e,f) verify that all Ni and O atoms actively take part in redox reactions with significantly increased atomic charges upon delithiation, while atomic charges of Mn just increase a little, which is consistent with the traditional understandings of redox inertness of the octahedral Mn in cathodes.[28,59] At the beginning of delithiations from $Li_{11}Ni_2Mn_5O_{18}$ to $Li_8Ni_2Mn_5O_{18}$, atomic charges of Ni rapidly increase, while atomic charges of Mn nearly keep a constant of +1.85e. From $Li_7Ni_2Mn_5O_{18}$ to final $Ni_2Mn_5O_{18}$, atomic charges of Ni and Mn increase a little. Figure 3g shows the bond lengths of Ni−O and Mn−O of $Li_{11-x}Ni_2Mn_5O_{18}$ with respect to different delithiation concentrations. Upon delithiation, bond lengths of Mn−O slowly decrease from $Li_{11}Ni_2Mn_5O_{18}$ to $Ni_2Mn_5O_{18}$, while bond lengths of Ni−O rapidly reduce from $Li_{11}Ni_2Mn_5O_{18}$ to $Li_8Ni_2Mn_5O_{18}$ and then slowly decrease from $Li_7Ni_2Mn_5O_{18}$ to $Ni_2Mn_5O_{18}$. These variation trends of Ni−O and Mn−O bond lengths are consistent with those of Ni and Mn atomic charges, firmly demonstrating the much higher redox activities of Ni than Mn.

For lattice oxygens, their atomic charges decrease almost linearly with the increase of delithiation concentration, as shown in Figure 3f, which demonstrate the significant oxidizations of lattice oxygen of $Li_{11}Ni_2Mn_5O_{18}$ upon delithiation. Importantly, it is noticed that the slope of oxygen Bader charges *vs* delithiation concentration of Li-honeycomb structures is larger than that of Ni-honeycomb structures, showing that more electrons taking part in redox processes. On the other hand, we integrated oxygen PDOS from −1.0 eV to 0 of $Li_{11-x}Ni_2Mn_5O_{18}$ at different delithiation levels, as shown in Figure 3h. Overall, Li-honeycomb structures have more O-2p occupied electrons close to the Fermi energy level than Ni-honeycomb structures. Therefore, it can be concluded that lattice oxygens in the Li-honeycomb structured $Li_{11-x}Ni_2Mn_5O_{18}$ have higher redox activities than Ni-honeycomb structures.

3.3. Oxygen Dimerization. Li extraction from the Li-rich Mn-based oxide cathodes has been demonstrated to be accompanied by oxidation of O^{2-} to O^-, forming oxygen dimers,[28,60] which would disorder the oxygen sublattice and trigger the TM atom migrating from the TM layer to the delithiated Li layer. In experiments, the capacity of first charging is close to the theoretical capacity of 350 mAh/g and the capacity of second charging is more than 300 mAh/g,[61,62] indicating that more than 1.03 Li^+ are reversibly reinserted into the crystal structure, and deeply delithiated structures $Li_xNi_{0.22}Mn_{0.56}O_2$ ($x < 0.2$) are actually available. The more the Li extraction, the easier the lattice oxygen dimerization will be.[63,64] Thus, in this work, we selected some deeply delithiated structures to efficiently examine how the Li−Mn−Ni cation configuration affects the thermodynamics and dynamics of oxygen dimerization, including Li-honeycomb and Ni-honeycomb structured $Li_xNi_{0.22}Mn_{0.56}O_2$ (x = 0, 0.11, and 0.33). This method of studying deeply delithiated structure using DFT is consistent with the previous work of Li_2MnO_3, in which fully delithiated MnO_3 was selected for DFT calculation of oxygen dimerization.[16]

Note that the macroscopical oxygen gas release and phase transformation are not considered for oxygen dimerization process in this work, but the probability and rate of TM migration were studied, including the calculations of formation energies and activation energy barriers for Mn and Ni atoms from the TM layer migrating to their adjacent Li vacancy sites along interlayer and intralayer directions in the fully delithiated $Ni_{0.22}Mn_{0.56}O_2$, as depicted in Figure 4. Viewed from Figure 4a, the formation energies of migrated Mn and Ni atoms after interlayer diffusion are usually lower than those of intralayer diffusion, indicating that Mn and Ni atoms prefer to occupy the Li vacancy layer in the fully delithiated $Ni_{0.22}Mn_{0.56}O_2$ structure. On the other hand, DFT structural optimizations show, for most cases, that Mn atoms firmly reside at the tetrahedral vacancy sites after migration, which is in good accordance with the previous work of Li_2MnO_3,[65] while Ni atoms still occupy at the octahedral vacancy sites after migration, as the final sites show in Figure 4c. For activation energy barriers (E_a) of Mn and Ni atom migration (Figure 4b), Mn and Ni atoms migrating along the interlayer direction usually have lower E_a than those along the intralayer direction. The lowest E_a of TM migration is 2.55 eV for Mn-5 interlayer diffusion with a negative formation energy of final tetrahedral Mn occupation in the Ni-honeycomb structure. It is worth noting that our calculated activation barriers for both Mn and

https://doi.org/10.1021/acsaem.3c00480
ACS Appl. Energy Mater. XXXX, XXX, XXX−XXX

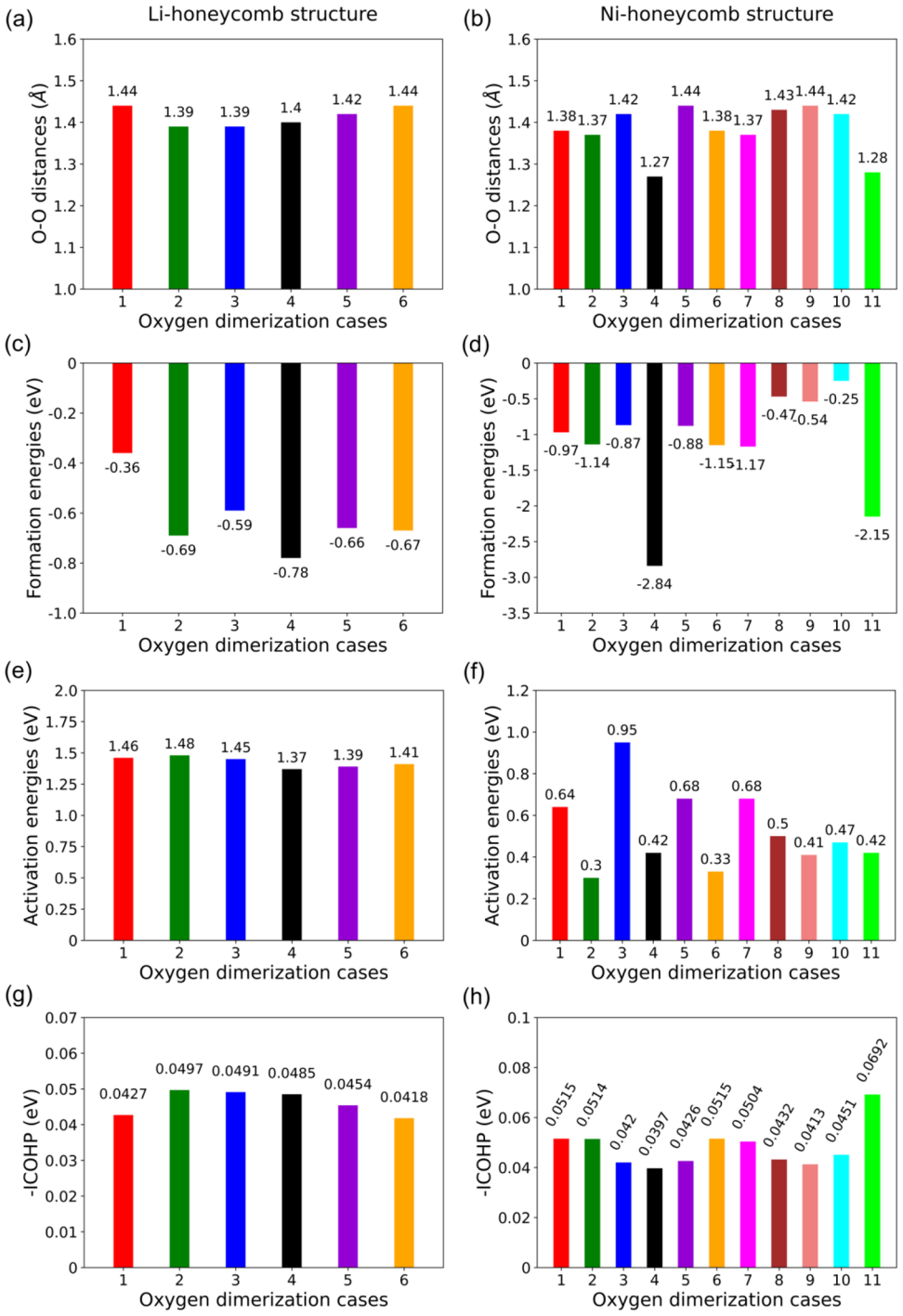

Figure 6. (a,b) O−O atomic distance (d_{O-O}, in Å), (c,d) formation energies (E_f, in eV), (e,f) activation energy barriers (E_a, in eV), and (g,h) −ICOHP values integral to the Fermi level for oxygen dimerization in the Li−Ni−Mn mixed intralayer of the fully delithiated Li-honeycomb and Ni-honeycomb structured $Ni_{0.22}Mn_{0.56}O_2$, respectively.

Ni migrations are quite high, which just demonstrate the low probability of TM migration in theory. There may be some deviations between calculation results and experimental observation. We hold that our calculation results cannot fully exclude the practical possibility of TM migration in $Li_xNi_{0.22}Mn_{0.56}O_2$. In this work, we mainly focus on the relative difference of TM migration between Li-honeycomb and Ni-honeycomb structured $Ni_{0.22}Mn_{0.56}O_2$, firmly concluding that Mn migration in the Ni-honeycomb structure is slightly easier than that in the Li-honeycomb structure. Additionally, we also noticed other relatively higher activation barriers from DFT calculation for TM migration in layered cathode, such as E_a of 2.5−4.4 eV for Ni migration in $LiNi_{0.8}Mn_{0.1}Co_{0.1}O_2$.[66] NEB calculations of TM migration may be sensitive to the supercell size, the Hubbard parameter, and the lithium concentration, which need our further careful exploration.

In $Li_{1.22}Ni_{0.22}Mn_{0.56}O_2$, according to the coordination environments, there are three different oxygen ions, including an O ion bonding to four Li ions and two TM ions (O−4Li−

https://doi.org/10.1021/acsaem.3c00480
ACS Appl. Energy Mater. XXXX, XXX, XXX−XXX

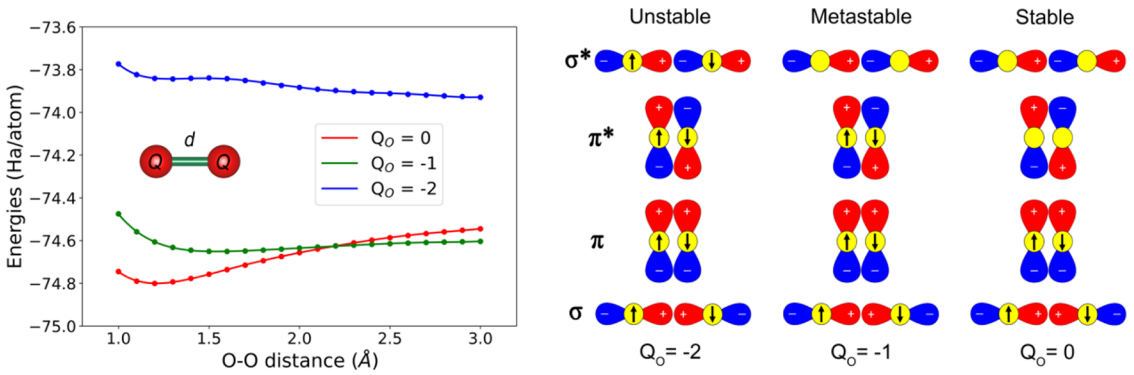

Figure 7. Stability of oxygen dimerization with respect to oxygen anion charge.

2TM), an O ion bonding to five Li ions and one TM ion (O−5Li−Ni−Mn), and an O ion bonding to three Li ions and three TM ions (O−3Li−3TM). Only these O atoms with O−4Li−2TM or O−5Li−Ni−Mn coordination environment showing Li−O−Li configuration have potentials for oxygen dimerization and oxygen redox.[12] For the fully delithiated Li-honeycomb $Ni_{0.22}Mn_{0.56}O_2$, all oxygen bond to two TM ions, distributing along the edge of Li vacancy in the Li−Ni−Mn mixed layer, as shown in Figure 5a. While for the fully delithiated Ni-honeycomb $Ni_{0.22}Mn_{0.56}O_2$, there are some oxygen ions bonding to only one TM ion, distributing along the edge of two adjacent Li vacancies in the Li−Ni−Mn mixed layer, as shown in Figure 5b.

Figure 5 shows the potential intralayer oxygen dimerization in the TM layer for the fully delithiated Li-honeycomb and Ni-honeycomb structured $Ni_{0.22}Mn_{0.56}O_2$. The calculated formation energies, activation energy barriers, and energy profiles of oxygen dimerization in the fully delithiated $Ni_{0.22}Mn_{0.56}O_2$ are listed in Figures 6 and S9 and S10. Viewed from Figure 6a,b, both for the Li-honeycomb and Ni-honeycomb structured $Ni_{0.22}Mn_{0.56}O_2$, all oxygen dimers with O−O distances less than 1.44 Å can be regarded as peroxides (O_2^{2-}), and some of them (1.27−1.39 Å) are further less than 1.40 Å, indicating the formation of superoxides (O_2^-).[16,67] It can be seen that all formation energies of oxygen dimerization (Figure 6c,d) are lower than zero, which means that oxygen dimerization is a thermodynamically spontaneous process in these fully delithiated structures. These thermodynamic driving forces for oxygen dimerization come from the enhanced oxidation degree of these electrons occupied in the σ^* and π^* O−O antibonding orbitals (increased valence state of the O ion), as shown in Figure 7. Two O^{2-} ions with four electrons occupying in the σ^* and π^* O−O antibonding orbitals tend to isolate from each other, corresponding to the unstable oxygen dimers. When O ions are further oxidized to a valence of −1 with an empty 2p-orbital, two O^- ions with no electron occupying in the σ^* O−O antibonding orbital start to bond with each other, forming (meta)stable O^-−O^- dimerization. In a word, more electrons extracted from oxygen ions would stabilize oxygen dimers, and the ultimate case is that two neutral O atoms would spontaneously form a O_2 molecule. All oxygen atomic Bader charges (Figure 3f) of the deeply delithiated $Li_xNi_{0.22}Mn_{0.56}O_2$ ($x < 2/3$) are more positive than −1, driving oxygen dimerization with short O−O atomic distances of ∼1.30 Å.

For dimerization dynamics (Figure 6e,f), activation energy barriers (0.30−0.95 eV) of oxygen dimerization in the Ni-honeycomb structured $Ni_{0.22}Mn_{0.56}O_2$ are much lower than those of Li-honeycomb structures and close to the fully delithiated MnO_3 of Li_2MnO_3.[16] In Ni-honeycomb structures, the variations of formation energy and activation energy barrier with respect to different locations of oxygen dimerization (case 1−11) are more remarkable than those in Li-honeycomb structures (case 1−6), showing that oxygen dimerization in Ni-honeycomb structures are more sensitive to the local coordination environment. Most importantly, all Ni-honeycomb structured $Ni_{0.22}Mn_{0.56}O_2$ have much more negative formation energies and smaller activation energy barriers than Li-honeycomb structures, which are in good accordance with the previous work of the delocalized Li@Mn_6 superstructure units enabling layer stability of Li-excess Mn-rich $Li_{13}Mn_{11}O_{24}$.[68] In other words, the delithiated $Li_xNi_{0.22}Mn_{0.56}O_2$ with the Ni-honeycomb configurations in the Li−Ni−Mn mixed layer shows higher driving forces and rates for oxygen dimerization than Li-honeycomb structures, regardless of their relatively lower redox activities. Furthermore, these activation energies would further decrease at the surface where the coordination number is lower or after subsequent oxygen dimers have formed.[69]

In Li-honeycomb structures, case-2, case-3, and case-4 correspond to the more negative formation energies and smaller O−O bond lengths for oxygen dimerization. According to the COHP analyses (Figures 6g and S11), these three integrated COHP (−ICOHP) values at the Fermi energy level of O−O bond are relatively larger than those of other cases, indicating that stronger O−O 2p orbital interactions make smaller O−O atomic distances for oxygen dimerization (Figure 6a), eventually leading to more negative formation energies. O1−O13 dimerization (case-4) corresponds to the lowest formation energy of −0.78 eV and the lowest activation energy barrier of 1.37 eV for oxygen dimerization, while for the fully delithiated Ni-honeycomb structured $Ni_{0.22}Mn_{0.56}O_2$, the situations are a bit complicated. Case-4 has the lowest formation energy of −2.84 eV and the smallest O−O distance of 1.27 Å for oxygen dimerization, while the corresponding activation energy barriers of 0.42 eV is the third lowest, same as case-11. Viewed from the local structure of oxygen dimerization of case-4 (Figure S12), two oxygen dimerizations of O5−O14 (1.45 Å) and O3−O12 (1.27 Å) are observed in the same structure, that is, forming O5−O14 oxygen dimerization would simultaneously arise O3−O12 oxygen dimerization (like case-11) in the fully delithiated Ni-honeycomb structured $Ni_{0.22}Mn_{0.56}O_2$. Thus, the formation energy of case-4 includes contribution of O3−O12 oxygen dimerization (like case-11), and case-4 can be regarded as the sum of O5−O14 and O3−O12 oxygen dimerizations. From

https://doi.org/10.1021/acsaem.3c00480
ACS Appl. Energy Mater. XXXX, XXX, XXX−XXX

COHP analyses in Figures 6h, S13 and S14, in Ni-honeycomb structures, it is also found that there is a good relationship between formation energy values (Figure 6b) and O−O bonding interactions for oxygen dimerization. Except for case-4, these five cases (1, 2, 6, 7, and 11) with relatively more negative formation energies usually have stronger O−O bonding interactions (larger −ICOHP values at the Fermi energy level). For case-11, forming O3−O12 oxygen dimerization would not simultaneously arouse O5−O14 oxygen dimerization (like case-4). In addition, each O atom (O3 and O12) in case-11 with the O−5Li−Mn configuration in Ni-honeycomb structures can provide two unpaired O-2p orbital overlapping (Figure S15) and doubling O−O bonding interactions, eventually making the most negative formation energy of O3−O12 dimerization. Moreover, O3−O15 dimerization (case-2) corresponds to the lowest activation energy barriers of 0.30 eV, which is very close to O2−O12 dimerization (case-6).

Putting more insights into these four cases (case-1, case-2, case-6, and case-7) with favorable formation energies, we find that one of the two O atoms in each oxygen dimerization is singly coordinated with one Mn and five Li (Figure 5b) and a dangling oxygen when being fully delithiated, named as O−5Li−Mn configuration, which is quite different from Li-honeycomb structures. For the aspects of activation energy barrier, case-1 and case-7 (0.64 and 0.68 eV) are about twice larger than case-2 and case-6 (0.30 and 0.33 eV). O10 in case-1 and O9 in case-7 bond to two different TM atoms (Mn and Ni), that is, O−4Li−Mn−Ni configuration. These much higher activation energy barriers of oxygen dimerization in case-1 and case-7 than those of case-2 and case-6 are due to rigidity (covalency) difference between Mn−O and Ni−O bonds, and the stronger covalent Ni−O is more rigid for hindering oxygen dimerization compared to Mn−O with stronger ionicity.[19,60,63,64]

Besides the fully delithiated $Ni_{0.22}Mn_{0.56}O_2$, oxygen dimerization in the not fully delithiated $Li_{0.33}Ni_{0.22}Mn_{0.56}O_2$ and $Li_{0.11}Ni_{0.22}Mn_{0.56}O_2$ were also investigated, and the corresponding structures and energy profiles of oxygen dimerization are shown in Figures S16 and S17. Similar to $Ni_{0.22}Mn_{0.56}O_2$, the activation energy barriers of oxygen dimerization in the Ni-honeycomb structured $Li_xNi_{0.22}Mn_{0.56}O_2$ (x = 0.33 and 0.11) are slightly smaller than those of Li-honeycomb structures. Activation energy barriers of oxygen dimerization reduce when delithiating from $Li_{0.33}Ni_{0.22}Mn_{0.56}O_2$ to $Li_{0.11}Ni_{0.22}Mn_{0.56}O_2$ then to $Ni_{0.22}Mn_{0.56}O_2$, in accordance with the previous work.[63,64] All formation energies of oxygen dimerization in $Li_{0.33}Ni_{0.22}Mn_{0.56}O_2$ are calculated to be positive, while 6 out of 20 cases of $Li_{0.11}Ni_{0.22}Mn_{0.56}O_2$ have negative formation energies. It means that there are no driving forces for oxygen dimerization when charging from $Li_{1.22}Ni_{0.22}Mn_{0.56}O_2$ to $Li_{0.33}Ni_{0.22}Mn_{0.56}O_2$, and oxygen dimerization mainly occurs at the last quarter period of charging from $Li_{0.33}Ni_{0.22}Mn_{0.56}O_2$ to $Ni_{0.22}Mn_{0.56}O_2$. Thus, recycling the $Li_{1.22}Ni_{0.22}Mn_{0.56}O_2$ cathode within three-quarters of theoretical capacity may effectively inhibit oxygen dimerization and even oxygen gas release.

Here, based on the comprehensive analyses of thermodynamics and dynamics of oxygen dimerization, it can be concluded that oxygen dimerization prefers to occur around those dangling oxygens only singly coordinated with Mn and far away from Ni in those Ni-honeycomb structures when charging from $Li_{0.33}Ni_{0.22}Mn_{0.56}O_2$ to $Ni_{0.22}Mn_{0.56}O_2$. The Ni-honeycomb Li−Ni−Mn cation configurations provide a fresh perspective for us to understand the unstable layered structure and transformation to the spinel structure upon delithiation. Avoiding Ni-honeycomb structures with more favorable oxygen dimerization and making full use of Li-honeycomb structures with better redox activities are very important to optimally design high-performance Li-rich Mn-based cathode materials. Appropriately lowering the synthesis temperature to inhibit Ni-honeycomb structures in thermodynamics is worthwhile to be further explored in experiments.

4. CONCLUSIONS

In this work, based on DFT calculations, we examined a local Ni-honeycomb Li−Ni−Mn cation configuration for Li-rich Mn-based $Li_{1.22}Ni_{0.22}Mn_{0.56}O_2$ cathode material. These local Ni-honeycomb structures can coexist with local Li-honeycomb structures in the experimentally synthesized $Li_{1.22}Ni_{0.22}Mn_{0.56}O_2$ samples because the simulated XRD pattern, the lattice constant response to delithiation, and the voltage profile during the discharging process of Ni-honeycomb structures are very close to the experimental data. NEB calculations show that the Ni-honeycomb structured $Ni_{0.22}Mn_{0.56}O_2$ have higher probabilities of Mn migrating and occupying the tetrahedral sites in the Li vacancy layer. Electronic structure and Bader charge analysis demonstrate that nickel and lattice oxygen of Li-honeycomb $Li_xNi_{0.22}Mn_{0.56}O_2$ have higher redox activities than Ni-honeycomb structures. Additionally, it is found that oxygen dimerization depends not only on the delithiation level but also on the Li−Ni−Mn cation configurations. Oxygen dimerizations are sensitive to local coordination environments and prefer to occur around those dangling oxygens only singly coordinated with Mn and far away from Ni in those Ni-honeycomb structures when deeply charging from $Li_{0.33}Ni_{0.22}Mn_{0.56}O_2$ to $Ni_{0.22}Mn_{0.56}O_2$. The deeply delithiated $Li_xNi_{0.22}Mn_{0.56}O_2$ (x < 0.33) with Ni-honeycomb configurations show higher driving forces and lower energy barriers for oxygen dimerization than Li-honeycomb structures. By making comparisons between Li-honeycomb and Ni-honeycomb structured $Li_{1.22}Ni_{0.22}Mn_{0.56}O_2$, there is no correlation between high lattice oxygen redox activities and easy oxygen dimerization, such as Li-honeycomb structure simultaneously having higher lattice oxygen redox activities and higher energy barriers for inhibiting oxygen dimerization. These fresh findings not only promote deep understanding of the TM atom migration, redox activities, and oxygen dimerization but also provide another perspective for optimal design for Li-rich Mn-based cathode materials.

■ ASSOCIATED CONTENT

Data Availability Statement

Data supporting the findings of this study are available from the corresponding author on reasonable request.

Supporting Information

The Supporting Information is available free of charge at https://pubs.acs.org/doi/10.1021/acsaem.3c00480.

Structure information of $Li_{1.22-x}Ni_{0.22}Mn_{0.56}O_2$; electronic structures (PDOS); energy profiles of O_2 dimerization; and COHP of oxygen dimerization (PDF)

https://doi.org/10.1021/acsaem.3c00480
ACS Appl. Energy Mater. XXXX, XXX, XXX−XXX

AUTHOR INFORMATION

Corresponding Authors

Mingbo Zheng − *College of Materials Science and Technology, Nanjing University of Aeronautics and Astronautics, Nanjing 210016, China*; Email: zhengmingbo@nuaa.edu.cn

Hong Zhu − *University of Michigan−Shanghai Jiao Tong University Joint Institute, Shanghai Jiao Tong University, Shanghai 200240, China*; orcid.org/0000-0001-7919-5661; Email: hong.zhu@sjtu.edu.cn

Yongyao Xia − *College of Materials Science and Technology, Nanjing University of Aeronautics and Astronautics, Nanjing 210016, China; Department of Chemistry and Shanghai Key Laboratory of Molecular Catalysis and Innovative Materials, Institute of New Energy, iChEm (Collaborative Innovation Center of Chemistry for Energy Materials), Fudan University, Shanghai 200433, China*; orcid.org/0000-0001-6379-9655; Email: yyxia@fudan.edu.cn

Authors

Zhenming Xu − *College of Materials Science and Technology, Nanjing University of Aeronautics and Astronautics, Nanjing 210016, China*; orcid.org/0000-0002-7039-3845

Junwu Tian − *College of Materials Science and Technology, Nanjing University of Aeronautics and Astronautics, Nanjing 210016, China*

Zhi Dou − *College of Materials Science and Technology, Nanjing University of Aeronautics and Astronautics, Nanjing 210016, China*

Yixi Lin − *College of Materials Science and Technology, Nanjing University of Aeronautics and Astronautics, Nanjing 210016, China*

Huiyu Duan − *College of Materials Science and Technology, Nanjing University of Aeronautics and Astronautics, Nanjing 210016, China*

Complete contact information is available at: https://pubs.acs.org/10.1021/acsaem.3c00480

Notes

The authors declare no competing financial interest.

ACKNOWLEDGMENTS

This work is supported by the Young Scientists Fund of the National Natural Science Foundation of China (22209074), the Fundamental Research Funds for the Central Universities (Nos. NS2022059, NS2021039), the Talent Research Startup Funds of Nanjing University of Aeronautics and Astronautics, the Jiangsu Funding Program for Excellent Postdoctoral Talent, and the Selected Funding for Scientific and Technological Innovation Projects for Overseas Students in Nanjing. This work is partially supported by the High Performance Computing Platform of Nanjing University of Aeronautics and Astronautics.

REFERENCES

(1) Pomerantseva, E.; Bonaccorso, F.; Feng, X.; Cui, Y.; Gogotsi, Y. Energy Storage: The Future Enabled by Nanomaterials. *Science* **2019**, *366*, 969.

(2) Baum, Z. J.; Bird, R. E.; Yu, X.; Ma, J. Lithium-Ion Battery Recycling—Overview of Techniques and Trends. *ACS Energy Lett.* **2022**, *7*, 712−719.

(3) Min, X.; Xu, G.; Xie, B.; Guan, P.; Sun, M.; Cui, G. Challenges of Prelithiation Strategies for Next Generation High Energy Lithium-Ion Batteries. *Energy Storage Mater.* **2022**, *47*, 297−318.

(4) Hu, E.; Yu, X.; Lin, R.; Bi, X.; Lu, J.; Bak, S.; Nam, K.-W.; Xin, H. L.; Jaye, C.; Fischer, D. A.; Amine, K.; Yang, X.-Q. Evolution of Redox Couples in Li- and Mn-Rich Cathode Materials and Mitigation of Voltage Fade by Reducing Oxygen Release. *Nat. Energy* **2018**, *3*, 690−698.

(5) Pearce, P. E.; Perez, A. J.; Rousse, G.; Saubanere, M.; Batuk, D.; Foix, D.; McCalla, E.; Abakumov, A. M.; Van Tendeloo, G.; Doublet, M. L.; Tarascon, J. M. Evidence for Anionic Redox Activity in a Tridimensional-Ordered Li-Rich Positive Electrode Beta-Li_2IrO_3. *Nat. Mater.* **2017**, *16*, 580−586.

(6) Zhu, Z.; Yu, D.; Yang, Y.; Su, C.; Huang, Y.; Dong, Y.; Waluyo, I.; Wang, B.; Hunt, A.; Yao, X.; Lee, J.; Xue, W.; Li, J. Gradient Li-Rich Oxide Cathode Particles Immunized against Oxygen Release by a Molten Salt Treatment. *Nat. Energy* **2019**, *4*, 1049−1058.

(7) Hua, W.; Wang, S.; Knapp, M.; Leake, S. J.; Senyshyn, A.; Richter, C.; Yavuz, M.; Binder, J. R.; Grey, C. P.; Ehrenberg, H.; Indris, S.; Schwarz, B. Structural Insights into the Formation and Voltage Degradation of Lithium- and Manganese-Rich Layered Oxides. *Nat. Commun.* **2019**, *10*, 5365.

(8) Sharifi-Asl, S.; Lu, J.; Amine, K.; Shahbazian-Yassar, R. Oxygen Release Degradation in Li-Ion Battery Cathode Materials: Mechanisms and Mitigating Approaches. *Adv. Energy Mater.* **2019**, *9*, No. 1900551.

(9) House, R. A.; Maitra, U.; Jin, L.; Lozano, J. G.; Somerville, J. W.; Rees, N. H.; Naylor, A. J.; Duda, L. C.; Massel, F.; Chadwick, A. V.; Ramos, S.; Pickup, D. M.; McNally, D. E.; Lu, X.; Schmitt, T.; Roberts, M. R.; Bruce, P. G. What Triggers Oxygen Loss in Oxygen Redox Cathode Materials? *Chem. Mater.* **2019**, *31*, 3293−3300.

(10) Urban, A.; Seo, D.-H.; Ceder, G. Computational Understanding of Li-Ion Batteries. *npj Comput. Mater.* **2016**, *2*, 16002.

(11) Kuan-Yu Lin, S. N.; Huang, H.-W.; Jiang, J.-C. Theoretical Insights on Alleviating Lattice-Oxygen Evolution by Sulfur Substitution in $Li_{1.2}Ni_{0.6}Mn_{0.2}O_2$ Cathode Material. *npj Comput. Mater.* **2022**, *8*, 210.

(12) Seo, D. H.; Lee, J.; Urban, A.; Malik, R.; Kang, S.; Ceder, G. The Structural and Chemical Origin of the Oxygen Redox Activity in Layered and Cation-Disordered Li-Excess Cathode Materials. *Nat. Chem.* **2016**, *8*, 692−697.

(13) Johannes, M. D.; Swider-Lyons, K.; Love, C. T. Oxygen Character in the Density of States as an Indicator of the Stability of Li-Ion Battery Cathode Materials. *Solid State Ionics* **2016**, *286*, 83−89.

(14) Marusczyk, A.; Albina, J.-M.; Hammerschmidt, T.; Drautz, R.; Eckl, T.; Henkelman, G. Oxygen Activity and Peroxide Formation as Charge Compensation Mechanisms in Li_2MnO_3. *J. Mater. Chem. A* **2017**, *5*, 15183−15190.

(15) McCalla, E.; Abakumov, A. M.; Saubanere, M.; Foix, D.; Berg, E. J.; Rousse, G.; Doublet, M. L.; Gonbeau, D.; Novak, P.; Van Tendeloo, G.; Dominko, R.; Tarascon, J. M. Visualization of O−O Peroxo-Like Dimers in High-Capacity Layered Oxides for Li-Ion Batteries. *Science* **2015**, *350*, 1516−1521.

(16) Chen, H.; Islam, M. S. Lithium Extraction Mechanism in Li-Rich Li_2MnO_3 Involving Oxygen Hole Formation and Dimerization. *Chem. Mater.* **2016**, *28*, 6656−6663.

(17) Armstrong, A. R.; Holzapfel, M.; Novak, P.; Johnson, C. S.; Kang, S. H.; Thackeray, M. M.; Bruce, P. G. Demonstrating Oxygen Loss and Associated Structural Reorganization in the Lithium Battery Cathode $Li[Ni_{0.2}Li_{0.2}Mn_{0.6}]O2$. *J. Am. Chem. Soc.* **2006**, *128*, 8694−8698.

(18) Zhao, E.; Li, Q.; Meng, F.; Liu, J.; Wang, J.; He, L.; Jiang, Z.; Zhang, Q.; Yu, X.; Gu, L.; Yang, W.; Li, H.; Wang, F.; Huang, X. Stabilizing the Oxygen Lattice and Reversible Oxygen Redox Chemistry through Structural Dimensionality in Lithium-Rich Cathode Oxides. *Angew. Chem., Int. Ed. Engl.* **2019**, *58*, 4323−4327.

(19) Charles, N.; Yu, Y.; Giordano, L.; Jung, R.; Maglia, F.; Shao-Horn, Y. Toward Establishing Electronic and Phononic Signatures of Reversible Lattice Oxygen Oxidation in Lithium Transition Metal Oxides for Li-Ion Batteries. *Chem. Mater.* **2020**, *32*, 5502−5514.

(20) Song, J. H.; Yoon, G.; Kim, B.; Eum, D.; Park, H.; Kim, D. H.; Kang, K. Anionic Redox Activity Regulated by Transition Metal in

Lithium-Rich Layered Oxides. *Adv. Energy Mater.* **2020**, *10*, No. 2001207.
(21) House, R. A.; Maitra, U.; Perez-Osorio, M. A.; Lozano, J. G.; Jin, L.; Somerville, J. W.; Duda, L. C.; Nag, A.; Walters, A.; Zhou, K. J.; Roberts, M. R.; Bruce, P. G. Superstructure Control of First-Cycle Voltage Hysteresis in Oxygen-Redox Cathodes. *Nature* **2020**, *577*, 502−508.
(22) Zhang, J.; Cheng, F.; Chou, S.; Wang, J.; Gu, L.; Wang, H.; Yoshikawa, H.; Lu, Y.; Chen, J. Tuning Oxygen Redox Chemistry in Li-Rich Mn-Based Layered Oxide Cathodes by Modulating Cation Arrangement. *Adv. Mater.* **2019**, *31*, No. 1901808.
(23) Ning, F.; Li, B.; Song, J.; Zuo, Y.; Shang, H.; Zhao, Z.; Yu, Z.; Chu, W.; Zhang, K.; Feng, G.; Wang, X.; Xia, D. Inhibition of Oxygen Dimerization by Local Symmetry Tuning in Li-Rich Layered Oxides for Improved Stability. *Nat. Commun.* **2020**, *11*, 4973.
(24) Lo, W. T.; Yu, C.; Leggesse, E. G.; Nachimuthu, S.; Jiang, J. C. Understanding the Role of Dopant Metal Atoms on the Structural and Electronic Properties of Lithium-Rich $Li_{1.2}Ni_{0.6}Mn_{0.2}O_2$ Cathode Material for Lithium-Ion Batteries. *J. Phys. Chem. Lett.* **2019**, *10*, 4842−4850.
(25) Zeng, D.; Cabana, J.; Bréger, J.; Yoon, W.-S.; Grey, C. P. Cation Ordering in $Li[Ni_xMn_xCo_{(1-2x)}]O_2$-Layered Cathode Materials: A Nuclear Magnetic Resonance (Nmr), Pair Distribution Function, X-Ray Absorption Spectroscopy, and Electrochemical Study. *Chem. Mater.* **2007**, *19*, 6277−6289.
(26) Cahill, L. S.; Yin, S. C.; Samoson, A.; Heinmaa, I.; Nazar, L. F.; Goward, G. R. 6Li NMR Studies of Cation Disorder and Transition Metal Ordering in $Li[Ni_{1/3}Mn_{1/3}Co_{1/3}]O_2$ using Ultrafast Magic Angle Spinning. *Chem. Mater.* **2005**, *17*, 6560−6566.
(27) Chen, L.; Su, Y.; Chen, S.; Li, N.; Bao, L.; Li, W.; Wang, Z.; Wang, M.; Wu, F. Hierarchical $Li_{1.2}Ni_{0.6}Mn_{0.2}O_2$ Nanoplates with Exposed {010} Planes as High-Performance Cathode Material for Lithium-Ion Batteries. *Adv. Mater.* **2014**, *26*, 6756−6760.
(28) Li, X.; Qiao, Y.; Guo, S.; Xu, Z.; Zhu, H.; Zhang, X.; Yuan, Y.; He, P.; Ishida, M.; Zhou, H. Direct Visualization of the Reversible O^{2-}/O^{-} Redox Process in Li-Rich Cathode Materials. *Adv. Mater.* **2018**, *30*, No. 1705197.
(29) He, W.; Guo, W.; Wu, H.; Lin, L.; Liu, Q.; Han, X.; Xie, Q.; Liu, P.; Zheng, H.; Wang, L.; Yu, X.; Peng, D. L. Challenges and Recent Advances in High Capacity Li-Rich Cathode Materials for High Energy Density Lithium-Ion Batteries. *Adv. Mater.* **2021**, *33*, No. e2005937.
(30) Blöchl, P. E. Projector Augmented-Wave Method. *Phys. Rev. B* **1994**, *50*, 17953−17979.
(31) Kohn, W.; Sham, L. J. Self-Consistent Equations Including Exchange and Correlation Effects. *Phys. Rev.* **1965**, *140*, A1133−A1138.
(32) Perdew, J. P.; Burke, K.; Ernzerhof, M. Generalized Gradient Approximation Made Simple. *Phys. Rev. Lett.* **1996**, *77*, 3865−3868.
(33) Dudarev, S. L.; Botton, G. A.; Savrasov, S. Y.; Humphreys, C. J.; Sutton, A. P. Electron-Energy-Loss Spectra and the Structural Stability of Nickel Oxide: An LSDA+U Study. *Phys. Rev. B* **1998**, *57*, 1505−1509.
(34) Gao, Y.; Wang, X.; Ma, J.; Wang, Z.; Chen, L. Selecting Substituent Elements for Li-Rich Mn-Based Cathode Materials by Density Functional Theory (DFT) Calculations. *Chem. Mater.* **2015**, *27*, 3456−3461.
(35) Hart, G. L. W.; Forcade, R. W. Algorithm for Generating Derivative Structures. *Phys. Rev. B* **2008**, *77*, No. 224115.
(36) Ong, S. P.; Richards, W. D.; Jain, A.; Hautier, G.; Kocher, M.; Cholia, S.; Gunter, D.; Chevrier, V. L.; Persson, K. A.; Ceder, G. Python Materials Genomics (Pymatgen): A Robust, Open-Source Python Library for Materials Analysis. *Comput. Mater. Sci.* **2013**, *68*, 314−319.
(37) Henkelman, G.; Jónsson, H. Improved Tangent Estimate in the Nudged Elastic Band Method for Finding Minimum Energy Paths and Saddle Points. *J. Chem. Phys.* **2000**, *113*, 9978−9985.
(38) Maintz, S.; Deringer, V. L.; Tchougreeff, A. L.; Dronskowski, R. Lobster: A Tool to Extract Chemical Bonding from Plane-Wave Based Dft. *J. Comput. Chem.* **2016**, *37*, 1030−1035.
(39) Yu, M.; Trinkle, D. R. Accurate and Efficient Algorithm for Bader Charge Integration. *J. Chem. Phys.* **2011**, *134*, No. 064111.
(40) Kim, J.-S.; Johnson, C. S.; Vaughey, J. T.; Thackeray, M. M.; Hackney, S. A.; Yoon, W.; Grey, C. P. Electrochemical and Structural Properties of $xLi_2M'O_3\cdot(1-x)LiMn_{0.5}Ni_{0.5}O_2$ Electrodes for Lithium Batteries (M′ = Ti, Mn, Zr; $0 \leq X \leqslant 0.3$). *Chem. Mater.* **2004**, *16*, 1996−2006.
(41) Thackeray, M. M.; Johnson, C. S.; Vaughey, J. T.; Li, N.; Hackney, S. A. Hackney Advances in Manganese-Oxide 'Composite' Electrodes for Lithium-Ion Batteries. *J. Mater. Chem.* **2005**, *15*, 2257−2267.
(42) Lu, Z.; Beaulieu, L. Y.; Donaberger, R. A.; Thomas, C. L.; Dahn, J. R. Synthesis, Structure, and Electrochemical Behavior of Li $[Ni_xLi_{1/3-2x/3}Mn_{2/3-x/3}]$ O2. *J. Electrochem. Soc.* **2002**, *149*, A778.
(43) Yang, X.; Wang, S.; Han, D.; Wang, K.; Tayal, A.; Baran, V.; Missyul, A.; Fu, Q.; Song, J.; Ehrenberg, H.; Indris, S.; Hua, W. Structural Origin of Suppressed Voltage Decay in Single-Crystalline Li-Rich Layered $Li[Li_{0.2}Ni_{0.2}Mn_{0.6}]O_2$ Cathodes. *Small* **2022**, *18*, No. e2201522.
(44) Zhuang, Y.; Bao, Y.; Zhang, W.; Guan, M. 1,4-Dicyanobenzene as Electrolyte Additive for Improve Electrochemical Performance of $Li_{1.2}Ni_{0.6}Mn_{0.2}O_2$ Cathode Materials in Lithium Metal Rechargeable Batteries. *Chem. Eng. Sci.* **2022**, *247*, No. 117082.
(45) Sun, J.; Sheng, C.; Cao, X.; Wang, P.; He, P.; Yang, H.; Chang, Z.; Yue, X.; Zhou, H. Restraining Oxygen Release and Suppressing Structure Distortion in Single-Crystal Li-Rich Layered Cathode Materials. *Adv. Funct. Mater.* **2021**, *32*, No. 2110295.
(46) Cui, S. L.; Gao, M. Y.; Li, G. R.; Gao, X. P. Insights into Li-Rich Mn-Based Cathode Materials with High Capacity: From Dimension to Lattice to Atom. *Adv. Energy Mater.* **2021**, *12*, No. 2003885.
(47) Shao, Q.; Gao, P.; Yan, C.; Gao, M.; Du, W.; Chen, J.; Yang, Y.; Gan, J.; Wu, Z.; Zhang, C.; Chen, G.; Zheng, X.; Lin, Y.; Jiang, Y.; Sun, W.; Liu, Y.; Gao, M.; Pan, H. A Redox Couple Strategy Enables Long-Cycling Li- and Mn-Rich Layered Oxide Cathodes by Suppressing Oxygen Release. *Adv. Mater.* **2022**, *34*, No. e2108543.
(48) Hu, S.; Pillai, A. S.; Liang, G.; Pang, W. K.; Wang, H.; Li, Q.; Guo, Z. Li-Rich Layered Oxides and Their Practical Challenges: Recent Progress and Perspectives. *Electrochem. Energy Rev.* **2019**, *2*, 277−311.
(49) Qiu, B.; Zhang, M.; Xia, Y.; Liu, Z.; Meng, Y. S. Understanding and Controlling Anionic Electrochemical Activity in High-Capacity Oxides for Next Generation Li-Ion Batteries. *Chem. Mater.* **2017**, *29*, 908−915.
(50) Sathiya, M.; Abakumov, A. M.; Foix, D.; Rousse, G.; Ramesha, K.; Saubanere, M.; Doublet, M. L.; Vezin, H.; Laisa, C. P.; Prakash, A. S.; Gonbeau, D.; VanTendeloo, G.; Tarascon, J. M. Origin of Voltage Decay in High-Capacity Layered Oxide Electrodes. *Nat. Mater.* **2015**, *14*, 230−238.
(51) Billaud, J.; Sheptyakov, D.; Sallard, S.; Leanza, D.; Talianker, M.; Grinblat, J.; Sclar, H.; Aurbach, D.; Novák, P.; Villevieille, C. Li/Fe Substitution in Li-Rich Ni, Co, Mn Oxides for Enhanced Electrochemical Performance as Cathode Materials. *J. Mater. Chem. A* **2019**, *7*, 15215−15224.
(52) Voronina, N.; Shin, M. Y.; Kim, H. J.; Yaqoob, N.; Guillon, O.; Song, S. H.; Kim, H.; Lim, H. D.; Jung, H. G.; Kim, Y.; Lee, H. K.; Lee, K. S.; Yazawa, K.; Gotoh, K.; Kaghazchi, P.; Myung, S. T. Hysteresis-Suppressed Reversible Oxygen-Redox Cathodes for Sodium-Ion Batteries. *Adv. Energy Mater.* **2022**, *12*, No. 2103939.
(53) Zang, Y.; Ding, C.-X.; Wang, X.-C.; Wen, Z.-Y.; Chen, C.-H. Molybdenum-Doped Lithium-Rich Layered-Structured Cathode Material $Li_{1.2}Ni_{0.6}Mn_{0.2}O_2$ with High Specific Capacity and Improved Rate Performance. *Electrochim. Acta* **2015**, *168*, 234−239.
(54) Li, Y.; Bai, Y.; Wu, C.; Qian, J.; Chen, G.; Liu, L.; Wang, H.; Zhou, X.; Wu, F. Three-Dimensional Fusiform Hierarchical Micro/Nano $Li_{1.2}Ni_{0.6}Mn_{0.2}O_2$ with a Preferred Orientation (110) Plane as a

https://doi.org/10.1021/acsaem.3c00480
ACS Appl. Energy Mater. XXXX, XXX, XXX−XXX

High Energy Cathode Material for Lithium-Ion Batteries. *J. Mater. Chem. A* **2016**, *4*, 5942−5951.
(55) Momma, K.; Izumi, F. Vesta3 for Three-Dimensional Visualization of Crystal, Volumetric and Morphology Data. *J. Appl. Crystallogr.* **2011**, *44*, 1272−1276.
(56) Xiong, F.; Yan, H. J.; Chen, Y.; Xu, B.; Le, J. X.; Ouyang, C. The Atomic and Electronic Structure Changes Upon Delithiation of $LiCoO_2$: From First Principles Calculations. *Int. J. Electrochem. Sci.* **2012**, *7*, 9390−9400.
(57) Takahashi, Y.; Kijima, N.; Dokko, K.; Nishizawa, M.; Uchida, I.; Akimoto, J. Structure and Electron Density Analysis of Electrochemically and Chemically Delithiated $LiCoO_2$ Single Crystals. *J. Solid State Chem.* **2007**, *180*, 313−321.
(58) Assat, G.; Tarascon, J.-M. Fundamental Understanding and Practical Challenges of Anionic Redox Activity in Li-Ion Batteries. *Nat. Energy* **2018**, *3*, 373−386.
(59) Roos, J.; Eames, C.; Wood, S. M.; Whiteside, A.; Islam, M. S. Unusual Mn Coordination and Redox Chemistry in the High Capacity Borate Cathode $Li_7Mn(BO_3)_3$. *Phys. Chem. Chem. Phys.* **2015**, *17*, 22259−22265.
(60) Zhao, E.; Zhang, M.; Wang, X.; Hu, E.; Liu, J.; Yu, X.; Olguin, M.; Wynn, T. A.; Meng, Y. S.; Page, K.; Wang, F.; Li, H.; Yang, X.-Q.; Huang, X.; Chen, L. Local Structure Adaptability through Multi Cations for Oxygen Redox Accommodation in Li-Rich Layered Oxides. *Energy Storage Mater.* **2020**, *24*, 384−393.
(61) Guan, H.; Yang, Y.; Luo, H.; Chen, H.; Zhou, H. Improved Electrochemical Performance of a $Li_{1.2}Ni_{0.6}Mn_{0.2}O_2$ Cathode by a Hydrothermal Method with a Metal−Organic Framework as a Precursor. *ACS Appl. Energy Mater.* **2021**, *4*, 2506−2513.
(62) Zhuang, Y.; Lei, Y.; Guan, M.; Du, F.; Cao, H.; Dai, H.; Zhou, Q.; Adkins, J.; Zheng, J. 4-Aminobenzoic Acid as a Novel Electrolyte Additive for Improved Electrochemical Performance of $Li_{1.2}Ni_{0.6}Mn_{0.2}O_2$ Cathodes Via in Situ Electrochemical Polymerization. *Electrochim. Acta* **2020**, *331*, No. 135465.
(63) Xie, Y.; Saubanère, M.; Doublet, M. L. Requirements for Reversible Extra-Capacity in Li-Rich Layered Oxides for Li-Ion Batteries. *Energy Environ. Sci.* **2017**, *10*, 266−274.
(64) Chen, Z.; Li, J.; Zeng, X. C. Unraveling Oxygen Evolution in Li-Rich Oxides: A Unified Modeling of the Intermediate Peroxo/Superoxo-Like Dimers. *J. Am. Chem. Soc.* **2019**, *141*, 10751−10759.
(65) Radin, M. D.; Vinckeviciute, J.; Seshadri, R.; Van der Ven, A. Manganese Oxidation as the Origin of the Anomalous Capacity of Mn-Containing Li-Excess Cathode Materials. *Nat. Energy* **2019**, *4*, 639−646.
(66) Li, X.; Gao, A.; Tang, Z.; Meng, F.; Shang, T.; Guo, S.; Ding, J.; Luo, Y.; Xiao, D.; Wang, X.; Su, D.; Zhang, Q.; Gu, L. Robust Surface Reconstruction Induced by Subsurface Ni/Li Antisites in Ni-Rich Cathodes. *Adv. Funct. Mater.* **2021**, *31*, No. 2010291.
(67) Tygesen, A. S.; Chang, J. H.; Vegge, T.; García-Lastra, J. M. Computational Framework for a Systematic Investigation of Anionic Redox Process in Li-Rich Compounds. *npj Comput. Mater.* **2020**, *6*, 65.
(68) Weiyuan Huang, C. L.; Qiu, J.; Li, S.; Chen, Z.; Chen, H.; Zhao, W.; Ren, G.; Li, X.; Zhang, M.; Pan, F. Delocalized $Li@Mn_6$ Superstructure Units Enable Layer Stability of High-Performance Mn-Rich Cathode Materials. *Chem* **2022**, *8*, 2163−2178.
(69) Nachimuthu, S.; Huang, H.-W.; Lin, K.-Y.; Yu, C.; Jiang, J.-C. Direct Visualization of Lattice Oxygen Evolution and Related Electronic Properties of $Li_{1.2}Ni_{0.6}Mn_{0.2}O_2$ Cathode Materials. *Appl. Surf. Sci.* **2021**, *563*, No. 150334.

https://doi.org/10.1021/acsaem.3c00480
ACS Appl. Energy Mater. XXXX, XXX, XXX−XXX